RESEARCH ARTICLE
Rising Stars
ADVANCED MATERIALS
www.advmat.de

Scalable Jet Swimmer Driven by Pulsatile Artificial Muscles and Soft Chamber Buckling

*Wenhui Chen, Shengan Yang, Chi Zhu, Yitao Cheng, Yutong Shi, Chunpeng Yu, and Ke Liu**

Cephalopods, such as squid and nautilus, achieve fast swimming by jetting water swiftly from their chambers, offering benefits in swimming speed, energy efficiency, and silent operation. Inspired by these animals, a scalable soft robotic jet swimmer that utilizes soft chamber buckling to enable rapid water jetting is proposed. The design incorporates three main components: the knotted artificial muscle (KAM), an origami-inspired soft chamber, and a custom control module. The KAM generates significant force and stroke with minimal self-weight, but its actuation speed is insufficient for propelling water. To address this limit, an origami-inspired soft chamber that buckles instantly when the KAM's pulling force reaches a critical threshold is designed, thereby amplifying actuation speed and enabling rapid water jetting. The control module periodically activates the KAM to tighten and release, facilitating effective pulsatile propulsion. Similar to Cephalopods, this design is scalable and robust. Effective swimming of two robots is demonstrated with drastically different sizes, achieving a top speed of 0.62 body length per second. We also show that the propulsion is minimally compromised even when the KAM is significantly damaged. To further enable guided locomotion, a shape memory alloy rudder is incorporated for steering via infrared stimulation. This work demonstrates successful pulsatile jet swimming through the integration of smart materials and smart structures, laying the groundwork for future innovations in underwater soft robotics.

1. Introduction

The various types of locomotion of aquatic animals[1–4] have inspired the development of environmentally friendly underwater robots and instruments.[5–11] Based on their living environments and predation strategies, aquatic animals exhibit four primary swimming modes: oscillatory, undulatory, drag-based, and pulsatile. Among these, pulsatile swimmers, including jellyfish, squid, and nautilus, are known for quietness, high swimming speed (relative to body length), and lower cost of transport.[12–14] This exceptional performance arises from the force generated by their impulsive motions, which produces significant thrust.[15–17] Recent efforts in underwater robots have primarily focused on realizing oscillatory, undulatory, and drag-based swimming modes,[18–22] as artificial muscles are not yet as effective as biological muscles for pulsatile swimming.[23–28]

The major challenge is to achieve sufficient discharge rate of water, and current developments have mostly focused on improving the actuation speed of artificial muscles.[29–35] Substantial efforts have been made to adjust material composition[36–38] and structure of artificial muscles.[39–42] Yet it has been overlooked that the discharge rate of water not only depends on the actuation speed of artificial muscles,[22,43–48] but also the structural design of the water chamber, as shown in other related researches.[32–35] For instance, a bistable structure releases artificial muscles' actuation force during fast state switching, enabling quick paddle flapping for swimming.[21] Therefore, our approach is to integrate intelligent design of the water chamber with efficient artificial muscles, in order to amplify the effective discharge rate.[22,43–46,48] We design an origami-inspired soft chamber that exhibits structural buckling under the pulling force of artificial muscles. Such buckling leads to sudden volumetric contraction, thereby significantly amplifies the discharge rate for effective water jetting.[21,49,50]

Based on the aforementioned approach, we propose a pulsatile jet swimmer that employs soft chamber buckling to amplify the actuation speed of knotted artificial muscles (KAMs), thereby facilitating effective propulsion. Our design is built

W. Chen, Y. Cheng, Y. Shi, K. Liu
School of Advanced Manufacturing and Robotics
Peking University
5 Yiheyuan Rd., Beijing 100871, China
E-mail: liuke@pku.edu.cn
S. Yang
Department of Mechanical Engineering
Stanford University
450 Jane Stanford Way, Stanford, CA 94305, USA
C. Zhu
School of Mechanics and Engineering Science
Peking University
5, Yiheyuan Rd., Beijing 100871, China
C. Yu
School of Mechanical and Aerospace Engineering
Nanyang Technological University
50 Nanyang Avenue, Singapore 639798, Singapore

The ORCID identification number(s) for the author(s) of this article can be found under https://doi.org/10.1002/adma.202503777

DOI: 10.1002/adma.202503777

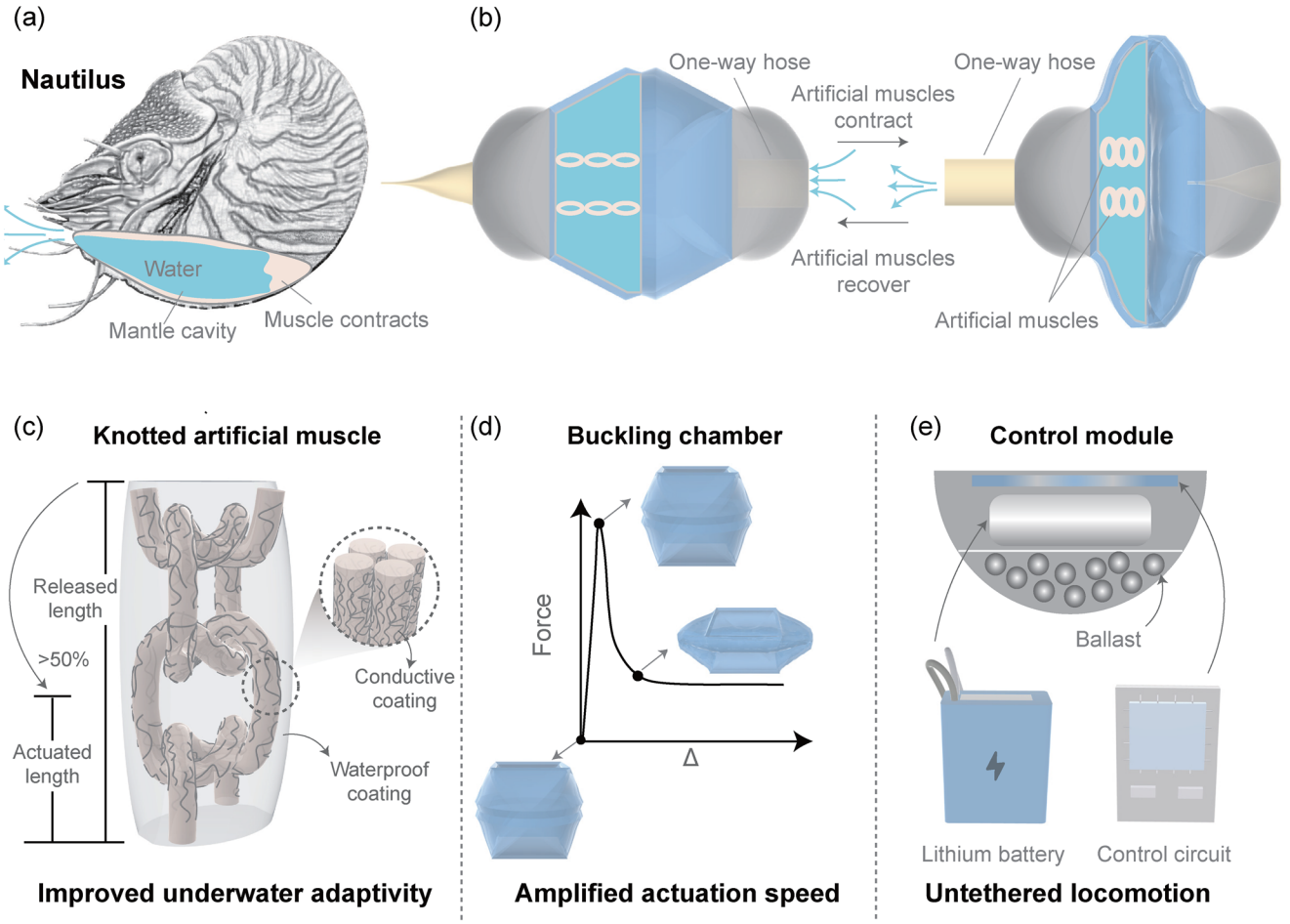

Figure 1. Design and characteristics of the bio-inspired pulsatile jet swimmer. a) The actuation mechanism of nautilus. b) Schematic of the bio-inspired pulsatile jet swimmer. Three major components of the jet swimmer are: c) the KAM for improved underwater adaptivity and large actuation strain; d) the soft buckling chamber for amplification of the actuation speed; and e) the on-board control module for untethered locomotion.

around three essential components: the KAMs, an origami-inspired soft chamber, and a custom control module. The KAM is braided from liquid crystal elastomer (LCE) fibers coated by conductive fibers, providing improved underwater actuation force and stroke that match the performance of biological muscles (**Figure 1c**), exhibiting both damage tolerance and scalability. While its actuation strain rate is inadequate to produce sufficient water discharge rate, we incorporate an origami-inspired soft chamber that buckles suddenly under the pulling of KAMs, boosting contraction speed and promoting rapid water jetting (Figure 1d). The custom control module powered by an onboard battery is used to stimulate the KAMs to periodically tighten and release (Figure 1e),[51,52] enabling untethered locomotion. Two rubbery one-way hoses are implemented as inlet and outlet of water to ensure unidirectional fluid flow. With these designs, the scalable jet swimmer demonstrates versatile performance: a peak speed of 0.62 body length (BL)/s when miniaturized and over 15 cm per cycle when scaled up, with minimal compromise in propulsion even KAMs are severely damaged. Furthermore, to realize guided movement, a shape memory alloy (SMA) rudder is integrated for steering, which can be activated by infrared stimulation. This study successfully demonstrates pulsatile jet swimming by integrating smart materials and smart structures, opening up new possibilities for designing adaptive, efficient, and quiet underwater robots capable of various missions, such as environmental monitoring and search-and-rescue.

2. Results and Discussion

2.1. Manufacturing and Actuation Performance of the KAM

We develop KAMs that serve as the actuator for the jet swimmer. The manufacturing process of these KAMs is outlined in **Figure 2a**. We leverage the centripetal force of a vortex to coat a conductive layer onto 3D-printed 500 μm LCE fibers. The conductive layer is a furry network formed by 7μm steel fibers (Figure S1, Supporting Information). The LCE fiber undergoes reversible, finite contraction with a transition temperature (T_{NI}) of 78 °C. To coat the steel fibers, a water vortex is created using a rotating magnet at 400 rpm. A fixed weight of steel fibers is then added into the water, where it rotates with the vortex and adheres to the surface of the LCE fiber (Movie S1, Supporting Information). Once the magnet stops rotating, the

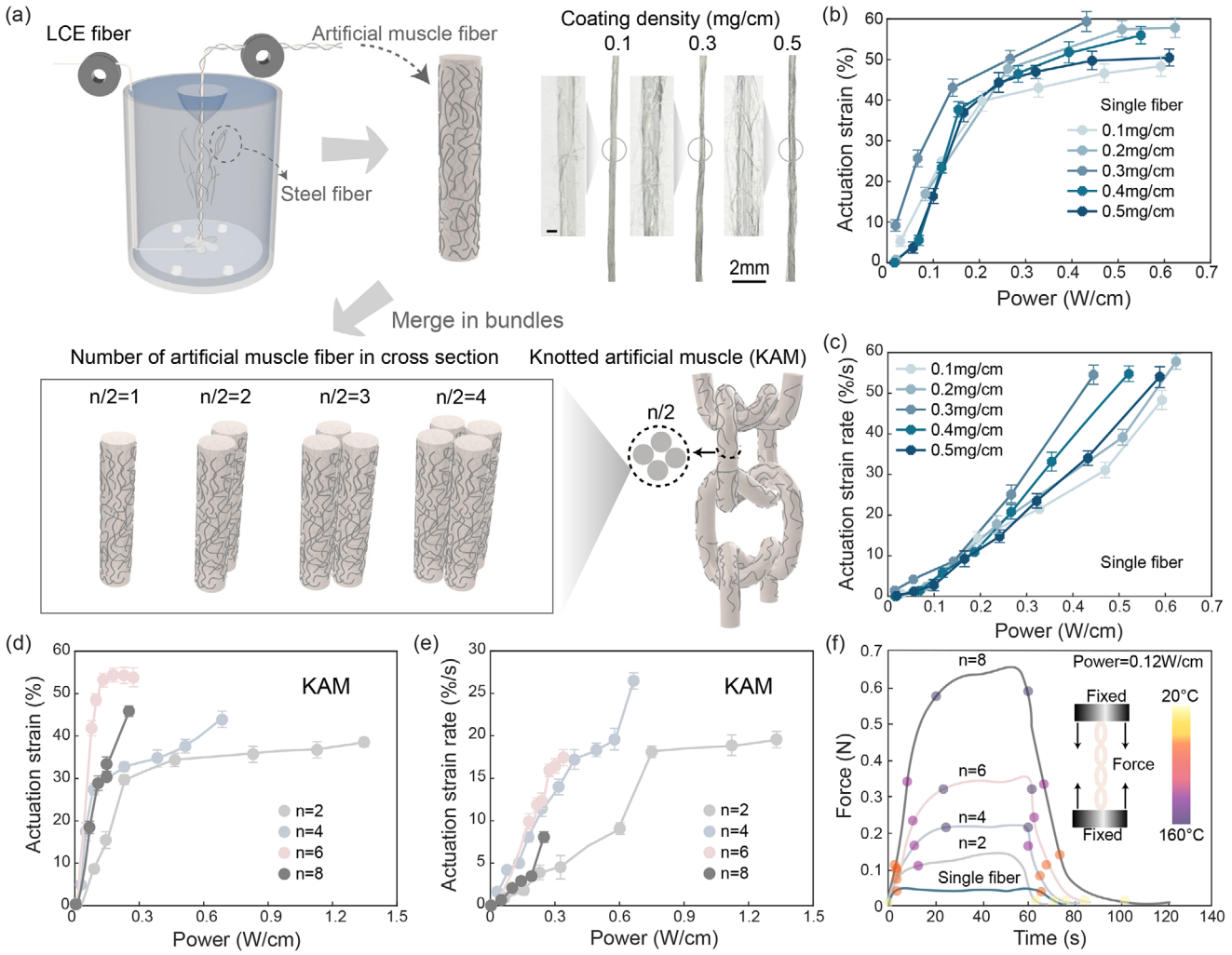

Figure 2. Manufacturing and actuation performance of the KAM. a) The manufacturing process of the KAM. The artificial muscle fibers are coated by extra thin steel fibers using a custom device. On the right we show zoom-in photographs of the coated furry conductive layer with different densities (scale bar is 200 μm). The fibers are then braided to form the KAM. b) The actuation strain and c) actuation strain rate of artificial muscle fibers with different coating densities versus input power. The error bars extend to one standard deviation. d) The actuation strain and e) actuation strain rate of the KAMs lifting a weight of 1g with different number of artificial muscle fibers in the cross section versus input power. The error bars extend to one standard deviation. f) The actuation force of the KAMs versus time with the input power of 0.12 Wcm^{-1}. The lines show the average values of three samples. The dots refer to the instant temperature of the KAMs.

water is wiped away from the LCE fiber's surface, and the steel fibers are gently kneaded to form a network that tightly wraps around the LCE fibers. When charged with electric current, the furry conductive layer generates heat, causing the LCE fiber to shrink. As we increase the coating density of the furry conductive layer from 0.1 to 0.3 mg cm^{-1}, both the actuation strain and strain rate of the artificial muscle fiber increase under the same power input (Figure 2b,c; Movie S2, Supporting Information). This improvement occurs because the higher density of conductive layer leads to lower electrical resistance and larger heating area (Figure S2a, Supporting Information). However, further increasing the density of conductive layer beyond 0.3 mg cm^{-1} leads to a decrease in actuation performance, which is likely due to extra mechanical stiffness of the steel fibers. Experiments show that the density of the conductive layer does not affect the heat dissipation, and therefore, does not influence the recovery speed of the artificial muscle fiber (Figure S2b, Supporting Information). As a result, we choose the density of the conductive layer to be 0.3mg cm^{-1}. The resultant artificial muscle fiber achieves an actuation strain of nearly 40% within one second, given power input of 0.4W cm^{-1} (Figure S2c, Supporting Information).

To scale up the actuation force, we bundle and braid the artificial muscle fiber into a square knot structure for additional structural contraction.[53,54] By varying the amount of fibers with a coating density of 0.3mg cm^{-1}, we create KAMs with different actuation performances and resistances (Figure S3a, Supporting Information). We denote the number of artificial muscle fibers in the cross section as n. When n increases from 2 to 6, both the actuation strain and strain rate improve, surpassing the performance of a single artificial muscle fiber. However, when n

further increases to 8, both the actuation strain and strain rate decrease. The decrease in actuation performance is attributed to the thickening of the bundle and the reduced space between the knots, which limit structural contraction during deformation (Figure 2d,e). The number of artificial muscle fibers in the cross-section of the KAM barely affects the heat dissipation rate. Thus, all KAMs display slower recovery speed than a single artificial muscle fiber (Figure S3b, Supporting Information). The actuation force of the KAMs increases as the number of fibers increases. Under the same power input of 0.12W cm^{-1}, the actuation force of a KAM with $n = 8$ in the cross-section reaches 0.66N, more than 12 times greater than the actuation force of a single artificial muscle fiber (Figure 2f). The accumulated heat induced by thicker cross section leads to such increase in actuation force (Figure S3c, Supporting Information). We also investigate the influence of the pitch distance between the knots on the actuation performance. When the distance between the knots are 10mm, we achieve optimal actuation strain over 60% (Figure S3c, Movie S3, Supporting Information). It is noteworthy that, as the KAM tightens, the resistance of conductive layer decreases owing to increased contact.

2.2. Underwater Actuation Performance of the KAM

Next, we explore the underwater actuation performance of the KAM. When submerged in water, a KAM with $n = 8$ under 5g load reaches an actuation strain of only 5% in 5s, while the same KAM achieves an actuation strain of 47% in air with the same power input (Figure S4, Supporting Information). The sharp decrease in actuation performance is caused by the high thermal conductivity of water, which leads to rapid heat dissipation from the KAM. For this reason, the actuation strain is improved to 35% by increasing the input power from 0.73 to 1.8W cm^{-1} (**Figure 3**a,b). However, further increases in heat input are constrained by the material's maximum tolerance, limiting the KAM's actuation strain to a maximum of 35%.

To mitigate the limitations in the underwater actuation performance of the KAM, we introduce a gummy waterproof coating made of uncured butyl rubber with a molecular weight of 10 000 (Figure 3b; Figure S5, Supporting Information). This gummy coating offers four key advantages. First, its liquid state allows the KAM to deform freely as before. Second, it does not react with water or LCE during heating, ensuring chemical stability. Third, its high molecular weight and viscous texture allow the coating to adhere firmly to the KAM, preventing leakage of water. Fourth, the heat dissipation coefficient of butyl rubber is significantly lower than that of water, effectively minimizing heat loss. After adding the waterproof coating, the KAM's underwater actuation strain increases to 55%, 1.6 times greater than that of the KAM without the coating (Figure 3a,b; Movie S4, Supporting Information). Additionally, the underwater durability of the KAM is significantly improved. Without the waterproof coating, prolonged exposure to water leads to LCE degradation and electrolysis of the conductive coating, causing the actuation to stop after approximately 675 cycles. In contrast, the waterproof KAM maintains functionality of high actuation strain even after more than 5000 cycles of heavy load lifting (Figure 3c; Figure S6, Movie S5,6, Supporting Information).

We stress that the waterproof KAM exhibits a higher energy density underwater compared to regular KAM in air (Figure 3d). Specifically, when lifting a weight approximately 900 times its own mass (100 g) (Figure 3e), the waterproof KAM achieves nearly 100 J kg^{-1}, almost double that of the regular KAM in air. This performance even surpasses the energy density of biological muscles.[55] In terms of power density, the waterproof KAM performs similarly to biological muscles[56] (Figure 3d; Figure S7, Supporting Information). Similar to the in-air case, we investigate the influence of the number of artificial muscle fibers in the KAM with various input power (Figure 3f). By increasing n from 8 to 16, the actuation force increases, reaching 1.5N with an input power of 2.5W cm^{-1}. However, further increasing n results in a trade-off: the actuation strain, strain rate, and recovery speed decrease to approximately 40%, 5%/s, and 3.8%/s, respectively (Figure S8, Supporting Information). When n exceeds 16, the actuation strain continues to decrease, leading to insufficient actuation strain. To find the optimal balance between actuation strain and force while minimizing energy input, we select the KAM with $n = 16$ for actuating the jet swimmer. This choice allows the KAM to be powered by a portable power source, which is important for untethered locomotion. Furthermore, the KAM demonstrates remarkable damage tolerance. Even under varying damage situations, the KAM retains the ability to deform. Notably, when two bundles are completely damaged, it can still achieve an underwater actuation strain of approximately 30%, ensuring continued functionality of the system (Figure 3g,h; Movie S7, Supporting Information).

Due to the unique design of the conductive layer and the addition of the waterproof coating, the KAM demonstrates leading underwater adaptability among soft artificial muscles. Compared to LCE- and hydrogel-based artificial muscles, our KAM exhibits superior underwater force density and energy density. Moreover, its excellent damage tolerance, combined with high underwater actuation force density, energy density, and actuation strain, outperforms that of dielectric elastomer (DE)-based artificial muscles (Figure S9, Supporting Information).

2.3. Design of the Soft Chamber

Although the conductive waterproof KAMs exhibit improved underwater adaptability, their actuation strain rates remain relatively low. To overcome this limitation, we design an origami-inspired soft chamber, which amplifies the KAM's actuation strain rate and enables rapid water jetting. As shown in the left panel of **Figure 4**a, the design aims to trigger the buckling of the soft chamber only when the KAM reaches a critical actuation force, thereby drastically reduces its volume to discharge water. The chamber remains undeformed until the pulling force of the KAM reaches a critical value.

We illustrate the actuation cycle and energy storage/release mechanism in the right panel of Figure 4a. From stage I to II, the KAM has not yet reached the critical buckling force, and the chamber remains almost undeformed. This corresponds to the energy storage phase, where energy is gradually building up as the KAM tightens. Once the actuation force of KAM exceeds a critical threshold (stage II), it triggers a sudden inward buckling of the chamber (stage II to III), resulting in a sharp and rapid

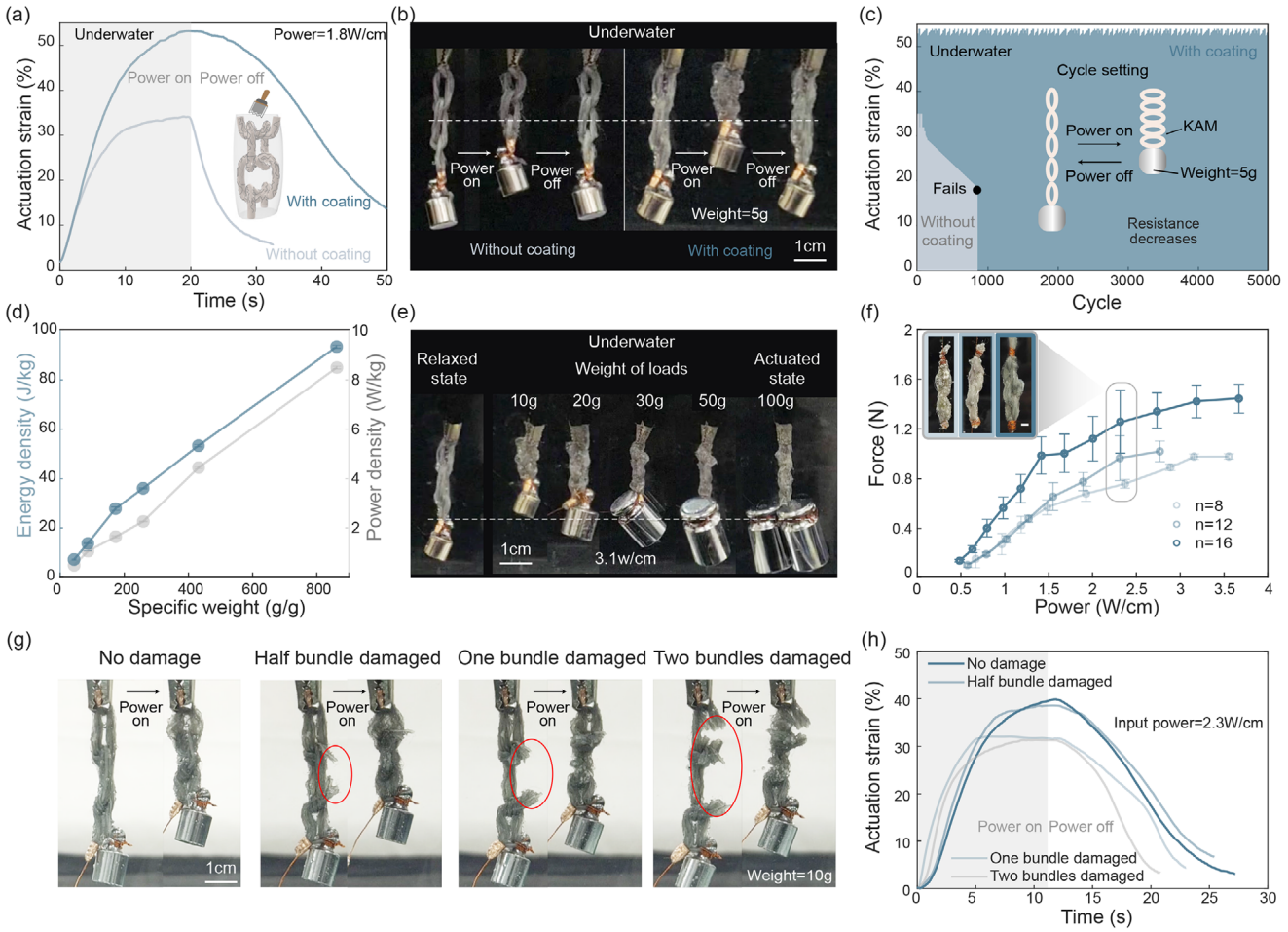

Figure 3. Underwater actuation performance of the KAM. a) The actuation performance of the KAM with and without the waterproof coating under an input power of 1.8W cm^{-1}. The lines represent the average values of three samples. The inset sketches the process of applying the waterproof coating to the KAM. b) Photographs of the KAM during the actuation with and without waterproof coating. c) Cyclic actuation of the KAM with and without the waterproof coating while lifting a 5g weight. The inset illustrates the cycle setting. d) The energy density and power density of the waterproof KAM underwater, plotted against specific weight. e) The relaxed state of the waterproof KAM hanging a 10g weight, and the actuated states of the KAM lifting weights of 10g, 20g, 30g, 50g, and 100g. f) The actuation force of the waterproof KAMs versus input power. The error bars represent one standard deviation. The inset shows the actuated states of different KAMs under input power of 2.2W (from left to right: $n = 8$, $n = 12$, $n = 16$). g) Photographs of undamaged and damaged KAMs lifting weights. h) The actuation process of undamaged/damaged KAM.

volume reduction. This is the energy release phase, during which the stored energy is quickly converted into propulsion of water. Because the buckling occurs rapidly, the contraction time of the chamber becomes much shorter than the total actuation time of the KAM.

The fabrication and design of the soft chamber are shown in Figures 4b and 4c, respectively. The chamber is molded using silicone gel material (see Experimental Section). The chamber features curved equator crease, defined by reduced thickness, enabling it to fold inward for water discharging. The geometry of the chamber is designed with the following relationships: $m = h$, $n = L/(2 - h)$, where m denotes the side length of the polar opening, h represents the height from the equator crease to the polar opening, and L denotes the arc length between points A and B, separated by the triangular ridges on the chamber (Figure 4c).

To enable faster contraction of the soft chamber, the deformation of the chamber before the trigger point shall be as small as possible, and the resistance force shall decrease rapidly after the trigger point. To achieve this goal, we conduct finite element analyses (FEA) (Figure S10, Supporting Information) to sweep different design parameters. The details of the FEA are provided in the Experimental Section. We adjust two structural parameters: $\alpha = G/L$ and $\beta = d_f/d_c$, where G is the width of the crease, d_f denotes the thickness of the chamber, and d_c denotes the thickness of the crease. We find that the deformation before the trigger point decreases as the parameter α decreases and β increases. Specifically, for $L = 3$cm, $h/L = 1/4$, and $d_f = 3$mm, the case of $\alpha = 1/10$ and $\beta = 1/3$ results in the smallest deformation before trigger point (Figure 4d,e). Additionally, the drop of the resistance force after the trigger point is most significant when $d_f = 3$mm (Figure 4f,g).

In summary, the FEA have allowed us to determine the optimal structural parameters for the buckling chamber: $\alpha = 1/10$, $\beta = 1/3$, $d_f = 3$mm, and $h/L = 1/4$ (Figure 4h). We prepare a set of molds by 3D printing to cast silicone gel into the

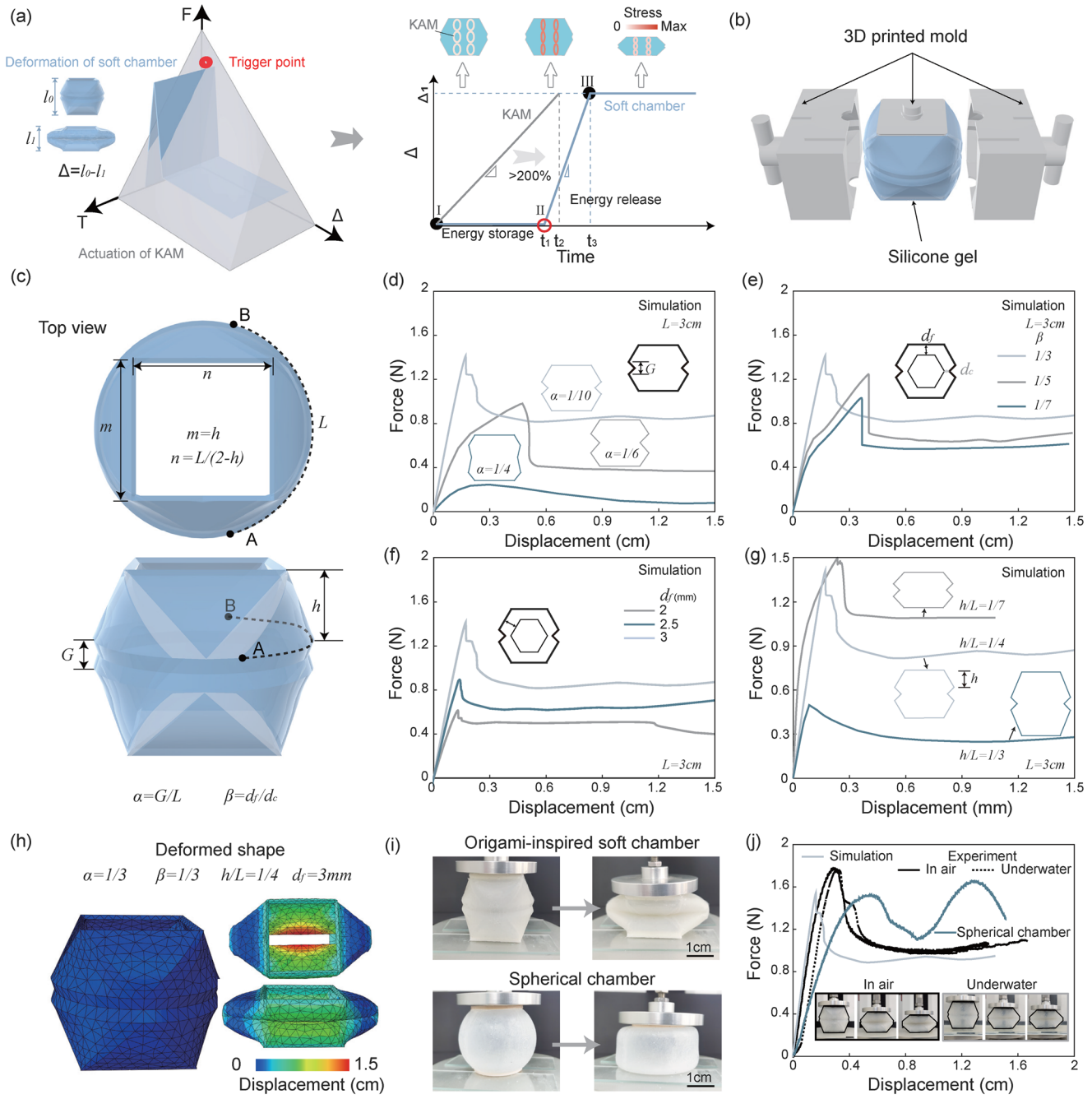

Figure 4. Design and optimization of the soft chamber. a) Design principle the soft chamber. The response surfaces of the soft chamber and the actuated KAM are shown in different colors. The insets show the definition of the compress distance, Δ. The right diagram illustrates how the soft chamber buckling amplifies the actuation speed of the KAM. The red circle refers to the trigger point of buckling. b) Schematic of the fabrication process of the soft chamber. c) Top and side views of the soft chamber. The shaded areas are the triangular ridges. d) Compression tests on the soft chamber with different α values. e) Compression tests of the soft chamber with different β values. f) Compression tests of the soft chamber with different d_f values. The inset shows the definition of d_f. g) Compression tests of the soft chamber with different h values. h) Images of the soft chamber before and after compression in finite element simulation. i) The photographs of the compression process of origami-inspired soft chamber and spherical chamber. j) Comparison of the compression behavior of the spherical chamber and the origami-inspired soft chamber in experiments (in air and underwater) and in simulation. The insets show the deformations in experiments. The simulation considers solid deformation only.

soft chamber with desired shape (Figure 4b). To ensure desired functionality, we first conduct a comparison experiment with a spherical chamber of the same size and wall thickness. During the compression process, the average compression force required for the spherical chamber is greater than that of our origami-inspired soft chamber. Additionally, the volume change of the spherical chamber is relatively uniform, lacking the rapid inward buckling and volume drop characteristics seen in the compression process of our origami-inspired chamber. As a result, the jetting speed and propulsion capability of the spherical chamber are significantly lower than those of our origami-inspired soft chamber (Figure 4i,j). We then conduct quasi-static compression tests on the silicone gel chamber in both air and underwater environments. The experimental results align well with the simulations (Figure 4j), showing that the origami-inspired soft chamber is now ready to be implemented on the jet swimmer.

2.4. Locomotion of the Scalable Pulsatile Jet Swimmer

Integrating the KAM with the soft chamber, we assemblei the propulsion device for the jet swimmer (**Figure** 5a). A sliding rack is added inside the soft chamber to prevent undesired deformation mode. Two one-way soft hoses are added to the two polar openings of the chamber, which ensures unidirectional flow of water during both the discharging and suction phases, facilitating efficient thrust generation. The one-way soft hoses are made of 0.02mm-thick rubber membrane with one end fixed and the other end free. Water could flow smoothly from the fixed end to the free end, but would be automatically blocked by the free end when flow backwards. When the KAM tightens, the soft chamber are pulled from inside to contract, causing the outlet hose to open and the inlet hose to close. Consequently, water inside the chamber is discharged through the outlet hose to form a water jet (Figure 5a). When the KAM releases, the soft chamber recovers to its original shape due to its inherent elasticity. During this process, the outlet hose closes, and the inlet hose opens, sucking in external water from the inlet hose. Repeating this cycle enables the jet swimmer to achieve unidirectional propulsion.

According to the literature,[12] the diameter of the hoses plays a crucial role in the propulsion of the jet swimmer. The volume of fluid exiting the outlet hose and entering the inlet hose can be approximated by two columns: one with length l_1 and diameter d_1 and another length l_2 and diameter d_2. The aspect ratio of fluid columns, defined as the stroke ratio $s = l_i/d_i$ (i = 1, 2), determines the characteristics of the water jet, which is stable and free of turbulence when the stroke ratio is between 1 and 4.[12] By equating the discharging volume V with the volume of the water jet, we obtain the expression for the diameters of the hoses (Equation 5, Supporting Information). The relationship between thrust F and the stroke ratio s is summarized by Equation S11 in the Supporting Information (Figure 5b). In order to get V, we substitute in the relation between the discharging volume V of the soft chamber and the compression distance Δ obtained from FEA (Figure 5b), along with the time duration obtained from experiments as described by Equation S12 and Equation S13 in Supporting Information (Figure S11b, Supporting Information). Using Equation S11 to Equation S13 in Supporting Information, we derive the relationship of discharging volume vs. time (Figure 5c), considering two different power sources: a tethered commercial power supply, and a customized untethered power supply using battery. Taking the derivative of V over time, we obtain the flow rate $\dot{V}$ as shown in Equation S11 in Supporting Information and find that F and s exhibit a positive monotonic correlation (Figure 5d). Therefore, the best propulsion efficiency is achieved when $s = 4$, with d_1 and d_2 determined to be approximately 1.0cm.

After determining all the design parameters of the propulsion device, we customize a control module to power the propulsion device. We employ constant current control, despite the fact that the resistance of the KAM decreases during tightening. We measure the average current and equivalent voltage on a known permanent resistor in the detection circuit. With these measured values, we calculate the resistance of the KAM and determine the equivalent voltage. The duty cycle of the pulse-width modulation (PWM) signal is then adjusted to change the equivalent voltage, ensuring a steady average current (Figures S11 and S12, Supporting Information). Details of the circuit design are provided in the Supporting Information. Finally, by integrating this circuit with a portable lithium battery, we construct the custom control module for the jet swimmer, which works as effectively as the commercial power supplies.

Next, we investigate the proper actuation input power and period. According to the relationship between the input power and the volume change of soft chamber during the discharging and suction processes, the time before trigger point shortens as the input power increases. When the input power exceeds 3.1W cm^{-1}, the waterproof coating on the KAM's surface begins to overheat and detach. As a result, we select 3.1W cm^{-1} as the optimal input power for the jet swimmer (Figure 5c,d; Movie S8, Supporting Information). With the input power of 3.1W cm^{-1}, we set the actuation period as 38s, with the power-on time T_1 lasting 20s to facilitate the buckling of the soft chamber. The power-off time T_2 lasts 18s for the elastic recovery of the soft chamber.

With the above actuation parameters, the jet swimmer experiences sufficient thrust during the buckling and recovery cycle (Figure 5e), enabling effective propulsion (Figure S11c, Supporting Information). The thrust in experiments is calculated using Equation S11 in Supporting Information, given an average input power of 3.1W cm^{-1} (Figure 5d). We conduct numerical simulation on one pulsatile cycle of the jet swimmer, considering fluid-structure interactions. The details of simulation is provided in the Experimental Section. The resulting thrust from the simulation matches the thrust calculated using experimental data during discharging. The discrepancy of thrust during suction is because we assume pure elastic behavior of the soft chamber in the simulation so that the suction duration is underestimated. The simulation verifies that both the buckling and recovery of the soft chamber generates notable accelerations through discharging and sucking water (Figures 5e; Movie S9, Supporting Information). The impulsive water jet is also uniform and stable, supporting our choice of the stroke ratio.

Building upon the validated thrust performance and stable actuation behavior, we further exploit the scalability of our jet swimmer design. This scalability allows us to explore two operational regimes: at smaller scales, the swimmer demonstrates fast swimming speed; at larger scales, it achieves untethered and

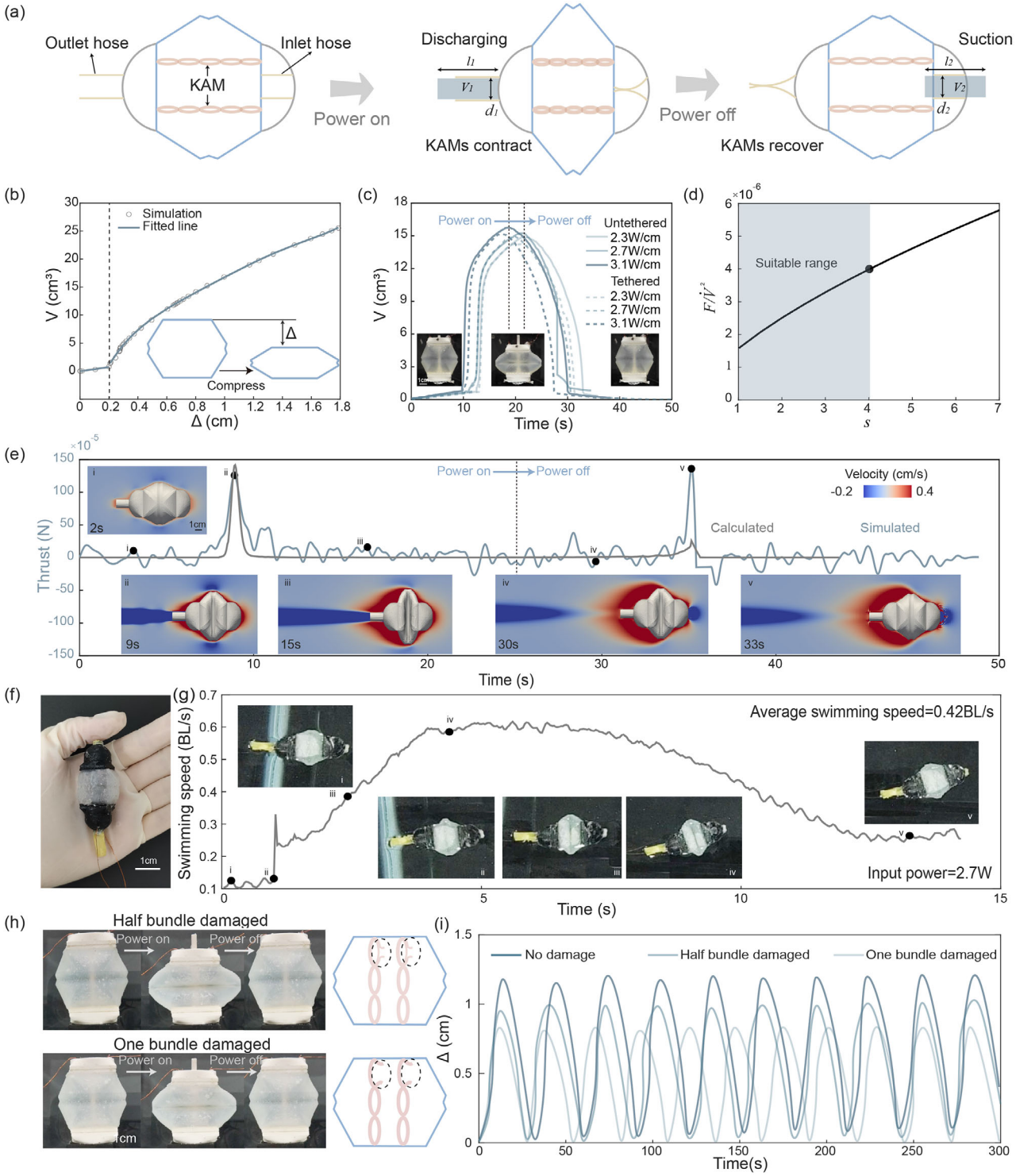

Figure 5. Analysis on the propulsion of the jet swimmer. a) The jetting mechanism of the propulsion device. b) The relationship between the discharging water volume of the soft chamber and the compression distance Δ during contraction of the soft chamber. The solid line represents the fitted curve. The inset illustrates the shape change during the contraction. c) The volume change versus time, under different power supplies. d) The relationship between weighted thrust F and stoke ratio s, as shown in Equation S11 in Supporting Information. The shaded area is the suitable range of stoke ratio. e) The thrust over time obtained from fluid simulation (blue line), and calculated from the experimental data (grey line). The insets show the magnitude of velocity of the fluid around the jet swimmer at different times. f) A photograph of the down-scaled jet swimmer. g) The swimming speed of the jet swimmer during one propulsion cycle. The insets show the states of the jet swimmer during the swimming process. h) Photographs of the deformation process of the soft chamber driven by damaged KAM. i) The underwater deformation cycle of the soft chamber pulled by undamaged KAM and damaged KAM.

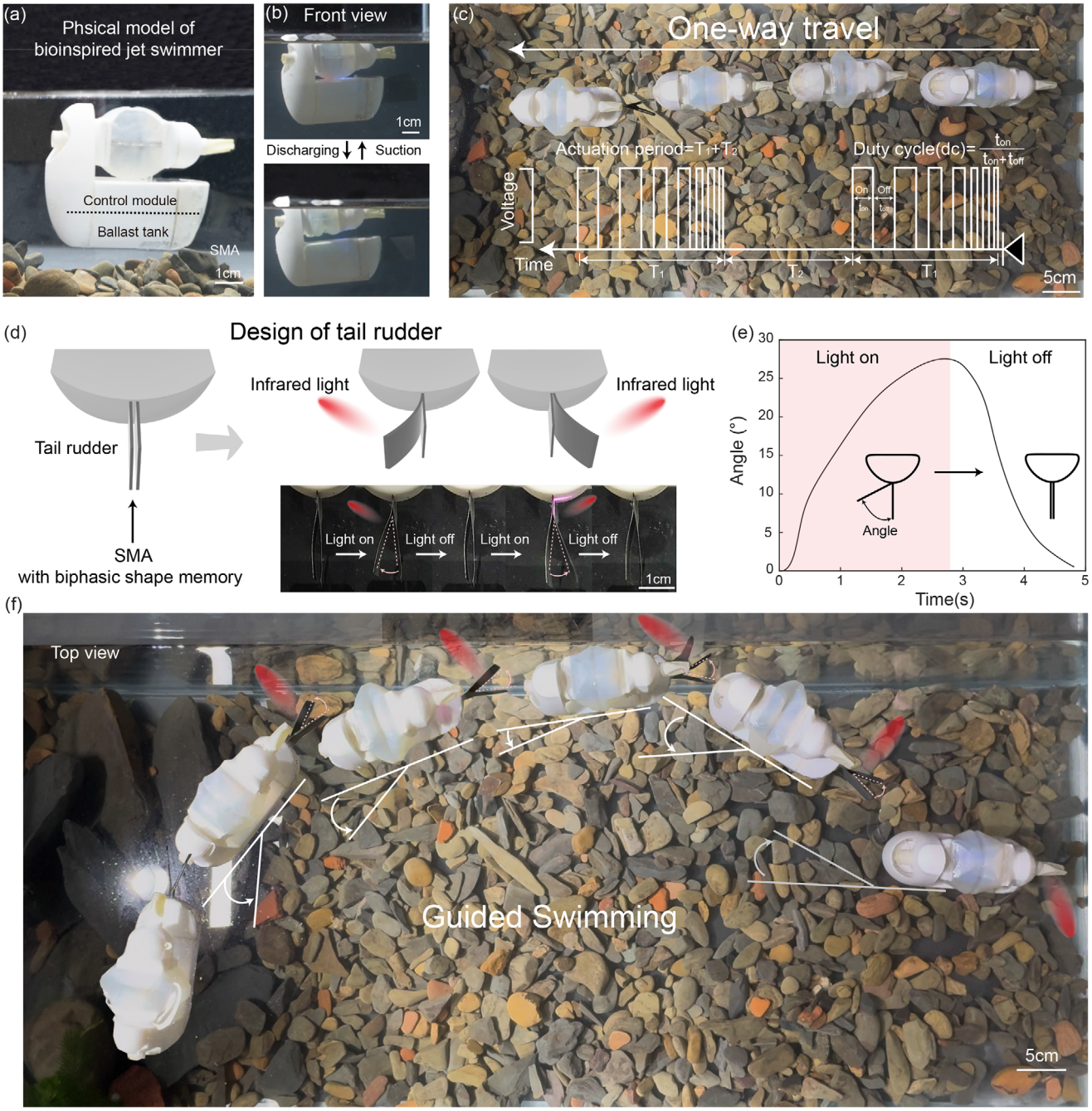

Figure 6. Underwater locomotion of the pulsatile jet swimmer. a) Photograph of the jet swimmer submerged in water. b) Discharging and suction process of the jet swimmer. c) One-way traveling of the jet swimmer. The inset shows the PWM control signal over time. The formula in the inset defines the duty cycle. d) Design of the SMA tail rudder and the steering mechanism. The insets show photographs of the tail rudder stimulated by infrared light on both sides. e) Change in the deflection angle of the tail rudder when infrared light is applied and stopped. f) Top views of the guided swimming of the jet swimmer. The red marks illustrate the incidences of external infrared light.

long-distance swimming performance. For instance, when the size of the soft chamber is reduced by half, the jet swimmer reaches a high speed of 0.62BL s^{-1} with 2.7W input power and achieves 20% energy conversion efficiency (Figure 5f,g; Movie S10, Supporting Information). In addition to scalability, the jet swimmer also possesses robustness that is not reported in existing jet robots. Even when the KAMs are damaged, they remain capable of reliably contracting the soft chamber (Figure 5h,i; Figure S14 and Movie S11, Supporting Information). To further demonstrate its practical applicability, we construct a fully untethered swimmer by integrating all functional components into a single system (**Figure 6**a,b). It is weighted 180g, actuated by two 0.3g KAMs (Figure 6b,c; Movie S12, Supporting Information). One pulsatile cycle demonstrates a propulsion distance of

15cm, approximately two times the body length of the swimmer. To enable guided movement of the jet swimmer, we incorporate a stimuli-responsive tail rudder. The rudder is made of two SMA films exhibiting a biphasic shape memory effect, activated at a transition temperature of 30°C (Figure 6d). When infrared light is spotted on one side of the tail rudder, the heating effect bends the SMA film to provide steering force. Once the light is removed, the rudder returns to its original straight shape. With an external infrared light power of 5W, the SMA film deflects by 30 degrees within 3s and returns to its original shape within 2s once the light if off (Figure 6e). This mechanism requires two of such films for steering into both left and right directions. By repeatedly stimulating one side of the tail rudder, the jet swimmer could make a U-turn. As shown in Figure 6f, under guided infrared light stimulation, the jet swimmer follows a trajectory close to a semicircle (Figure 6f; Movie S13, Supporting Information). The current use of infrared light aims to conceptually demonstrate the feasibility of thermal steering via SMA. In practical applications, the SMA rudder can be electrically controlled through compact onboard circuits. Future integration with control boards and wireless modules (e.g., Bluetooth) would enable fully autonomous or remotely guided navigation, supporting scalable and real-world deployment of the system.

Compared to other robotic jet swimmers, our design uniquely combines scalability and robustness. The use of soft artificial muscles rather than traditional motors enables inherent scalability, allowing the swimmer to adapt across various sizes and application scenarios. Even when the KAM is severely damaged, the swimmer continues to operate effectively, highlighting its robustness – a rare yet valuable trait in soft robotics (Table S1, Supporting Information). This scalable and robust design expands the functional scope of soft underwater robots, offering a versatile platform for future development in bio-inspired underwater robotics.

3. Conclusion

Inspired by natural pulsatile jet swimmers like the nautilus, we develop a scalable robotic jet swimmer, which is featured by a soft chamber that buckles to amplify jetting speed. Owing to the scalability of the design, the jet swimmer can adapt across different sizes, achieving a high-speed performance of 0.62BL s^{-1} when miniaturized, and long-distance propulsion of 15cm/cycle when scaled up. Notably, its propulsion performance remains largely unaffected even when the artificial muscles are significantly damaged. The jet swimmer' propulsion is powered by a novel design strategy, which integrates the KAM, soft chamber, and on-board control module. The LCE-based KAM with the conductive layer and the waterproof coating exhibits large underwater actuation force and stroke. The origami-inspired soft chamber buckles to amplify the KAM's actuation strain rate and accelerate water jetting. The whole system can be easily controlled by on-board control module and battery to enable untethered locomotion.

Our work demonstrates the successful integration of smart materials and smart structures in a robotic system, offering a promising pathway for developing efficient, adaptable, and intelligent underwater soft robots. This integration has further potential to enhance control accuracy, energy efficiency, and functionality, thereby expanding the robots' capabilities for advanced underwater functionality. Future research could involve equipping the jet swimmer with the abilities of autonomous decision-making, autonomous navigation, and tolerance to extreme depth, fulfilling complex tasks such as coral reef monitoring and search-and-rescue in challenging underwater environments.

4. Experimental Section

Detailed procedures are provided in the Supporting Information.

Preparation of the LCE ink: LCE ink was made by mixing (1,4-Bis-[4-(3-acryloyloxypropyloxy) benzoyloxy]-2-methylbenzene) (RM257) (Wilshire Technologies,95%), EDDET (Sigma-Aldrich, 95%), dipropylamine (Sigma-Aldrich, 98%), (2-hydroxyethoxy)-2-methylpropiophenone (Irgacure 2959, Sigma-Aldrich, 98%), RhB (Sigma-Aldrich), and methylene chloride (Sinopharm, CH2Cl2). RM257 (HWRK Chem, 8.2404g, 14mmol) was dissolved in 50mL of dichloromethane. Then, chain extender EDDET (2.1876g, 12mmol) and catalyst dipropylamine (0.100g, 1 mmol) were added into the mixture dropwisely. The solution was stirred at room temperature overnight. After that, a photoinitiator (Irgacure 651, Medkoo, 0.0500g, 0.2mmol) was added into the solution. Then, the mixture is left in an oven of 100°C for 24 h to allow complete evaporation of the solvent.

3D Printing of LCE Fiber: LCE ink is loaded into a syringe, which is then mounted on a customized direct ink writing 3D printer. LCE fibers are printed at a speed of 2mm s^{-1} at a room temperature of 25°C. The flow rate is controlled by regulating the air pressure to 80psi. After printing, the fibers are removed from the build plate and placed under a UV lamp with a wavelength of 365 nm for 1h of curing.

Fabrication of LCE Fiber Covered by Conductive fur and Knotted Artificial Muscle: We first prepare a perforated plate made by 3D printing, through which the LCE fiber is threaded. The plate is then fixed at the bottom of the 100mL-beaker to ensure that the LCE fiber remains continuously at the center of the vortex (Figure 2a). Next, 80mL of water is added to the beaker to create a water spiral. A magnet is placed in the beaker, and the magnetic stirrer is started, set to 400rpm. Using tweezers, the quantitatively weighed conductive fur is carefully inserted into the water spiral, where it rotates with the spiral. The centripetal force causes the conductive fur to wrap around the outside of the LCE fiber. After switching off the magnetic stirrer, the LCE fiber is then pulled out of the water, dried with dust-free paper, and forms a conductive coating. This process is repeated: the magnetic stirrer is switched on again, the conductive fur are inserted into the spiral, and once the stirrer is turned off, the LCE fibers are pulled out, dried, and twisted. By repeating this process, long fibers with conductive coatings of varying lengths can be continuously prepared. After obtaining LCE fibers coated with conductive fur and combining them into a single strand, they can be braided into a square knot structure to form a KAM.

Characterization of the LCE Ink: The DSC measurement is conducted using a Discovery DSC250 instrument (TA Instruments) under a nitrogen atmosphere. The heating and cooling processes were performed at a scanning rate of 40°C min^{-1}, spanning a temperature range from −20°C to 200°C (Figure S1, Supporting Information).

Actuation Characterization of the KAM: The actuation force of the knotted artificial muscle is tested using a Universal Mechanical Testing System (Series F, Mark-10) with a 50N load cell. By fixing the ends of the artificial muscle and keeping it in place, the actuation force can be measured under different power inputs after energizing the muscle.

A precision variable power supply (2200-50-3, ITECH) serves as the power source for the knotted artificial muscle bundles. Position and actuation are tracked using digital video or time-lapse photography with MATLAB. The temperature change during the actuation process is measured with an infrared thermal camera (PS400, GUIDE INFRARED). The water temperature during the shallow water actuation experiments is 18°C.

Fabrication of Origami-Inspired Soft Chamber: The molds for the origami-inspired soft chamber and dog-bone samples are prepared by 3D printing with polylactic acid (PLA) filament. First, we mix Ecoflex 00-20 elastomer (Smooth-On Inc.) in a 1:1 mass ratio, and remove air bubbles using a vacuum pump. Then, we pour the elastomer mixture into

the molds. After 8 h of curing, the molds are removed to obtain the final sample.

Material Characterization of the Soft Chamber: The dog-bone-shaped elastomer samples are stretched using the Universal Mechanical Testing System at a speed of 10mm/min to determine their mechanical properties.

Fabrication of the Control Module: The control module consists of a custom-designed circuit board, a lithium battery, and ballast. The circuit board was specifically designed by our team, with the design principles detailed in the Supporting Information. The custom lithium battery provides a stable output voltage of 14.8V and a capacity of 330mAh, which is sufficient to power the jet swimmer for over 10 min of continuous operation, allowing it to swim a total distance of more than 5m without noticeable degradation in performance. The ballasts are compact stainless steel balls.

Numerical Simulations: To optimize the shape parameters of the origami-inspired soft chamber, we conduct parametric FEA simulation studies. These simulations are carried out using the commercial FEA software Abaqus with the Abaqus/Standard solver. Geometric models of the chambers, created in Rhino, are imported into Abaqus CAE as STEP files and meshed using solid quadratic tetrahedral elements (C3D10). The elastomer is modeled as a hyperelastic isotropic material using the Yeoh model, and the mechanical properties are defined based on tensile test results from dog-boneshaped elastomer samples.

In addition to the FEA simulations, we employ the Immersed Boundary Method (IBM) for numerical simulation of fluid-structure interactions.[57] The fluid-structure coupling is modeled using a one-way coupling approach: the structure's kinematics are prescribed based on the simulated buckling deformation of the soft chamber, while the fluid flow is simulated in response. The computational domain is set at 10cm x 8cm x 30cm with a grid resolution of 100 x 80 x 300, resulting in approximately 2.4 million grid points. Time-stepping is implemented with a step size of 0.008 s during the contraction phase and 0.004s during the relaxation phase to ensure proper resolution of the transient dynamics.

Supporting Information

Supporting Information is available from the Wiley Online Library or from the author.

Acknowledgements

This research was supported by the National Key Research and Development Program of China through grant 2022YFB4701900, the National Natural Science Foundation of China through grant 12372159, Opening fund of State Key Laboratory of Nonlinear Mechanics and the College of Engineering of Peking University. The Analytical Instrumentation Center of Peking University is acknowledged for the measurements of DSC.

Conflict of Interest

The authors declare no competing interests.

Author Contributions

W.C. and K.L. designed the research. W.C., S.Y., Y.C., Y.S., and C.Y. performed all experiments. W.C. and S.Y. performed data analysis. W.C. and C.Z. conducted the theoretical derivations and numerical simulations. K.L. supervised the project. All the authors participated in the analysis of the results and in the writing of the paper.

Data Availability Statement

The data that support the findings of this study are available from the corresponding author upon reasonable request.

Keywords

artificial muscles, buckling, jet swimmer, origami-inspired structure, soft robot, underwater robot

Received: February 24, 2025
Revised: May 17, 2025
Published online:

[1] J. E. Colgate, K. M. Lynch, *IEEE J. Oceanic Eng.* **2004**, *29*, 660.
[2] P. Lutz, J. Musick, J. Wyneken, *The Biology of Sea Turtles, Volume II*, 1st edn., CRC Press, **2002**.
[3] J. O. Dabiri, S. P. Colin, K. Katija, J. H. Costello, *J. Exp. Biol.* **2010**, *213*, 1217.
[4] M. Gazzola, M. Argentina, L. Mahadevan, *Nat. Phys.* **2014**, *10*, 758.
[5] Z. Ren, W. Hu, X. Dong, M. Sitti, *Nat. Commun.* **2019**, *10*, 2703.
[6] T. Wang, H.-J. Joo, S. Song, W. Hu, C. Keplinger, M. Sitti, *Sci. Adv.* **2023**, *9*, eadg0292.
[7] T. Bujard, F. Giorgio-Serchi, G. D. Weymouth, *Sci. Rob.* **2021**, *6*, eabd2971.
[8] G. Arrick, D. Sticker, A. Ghazal, Y. Lu, T. Duncombe, D. Gwynne, B. Mouridsen, J. Wainer, J. P. H. Jepsen, T. S. Last, D. Schultz, K. Hess, E. Medina De Alba, S. Min, M. Poulsen, C. Anker, P. Karandikar, H. D. Pedersen, J. Collins, N. E. Egecioglu, S. Tamang, C. Cleveland, K. Ishida, A. H. Uhrenfeldt, J. Kuosmanen, M. Pereverzina, A. Hayward, R. K. Kirk, S. You, C. M. Dalsgaard, et al., *Nature* **2024**, *636*, 481.
[9] M. Ilami, H. Bagheri, R. Ahmed, E. O. Skowronek, H. Marvi, *Adv. Mater.* **2021**, *33*, 2003139.
[10] H. Yin, Y. Cao, B. Marelli, X. Zeng, A. J. Mason, C. Cao, *Adv. Mater.* **2021**, *33*, 2170156.
[11] A. K. Othman, D. A. Zekry, V. Saro-Cortes, K. J. P. Lee, A. A. Wissa, *Communications Engineering* **2023**, *2*, 30.
[12] T. V. Buren, D. Floryan, A. J. Smits, in *Bioinspired Structures and Design*, Cambridge University Press, **2020**, pp. 113–139.
[13] F. E. Fish, *Physiol. Biochem. Zool.* **2000**, *73*, 683.
[14] A. P. Hoover, N. W. Xu, B. J. Gemmell, S. P. Colin, J. H. Costello, J. O. Dabiri, L. A. Miller, *Proc. Natl. Acad. Sci. USA* **2021**, *118*, e2020025118.
[15] A. Glezer, M. Amitay, *Annu. Rev. Fluid Mech.* **2002**, *34*, 503.
[16] S. Ichikawa, O. Mochizuki, *J. Visualization* **2008**, *11*, 257.
[17] J. Yu, M. Tan, *Motion Control of Self-propelled Robotic Jellyfish*, Springer Singapore, Singapore, ISBN 978-981-13-8771-5, **2020**, pp. 173–196.
[18] J. Gu, J. Wang, Z. Liu, M. Tan, J. Yu, Z. Wu, *IEEE Trans. Rob.* **2025**, *41*, 159.
[19] B. Lu, C. Zhou, J. Wang, Y. Fu, L. Cheng, M. Tan, *IEEE Rob. Autom. Lett.* **2022**, *7*, 834.
[20] D. Wei, S. Hu, Y. Zhou, X. Ren, X. Huo, J. Yin, Z. Wu, *IEEE Rob. Autom. Lett.* **2023**, *8*, 6099.
[21] T. Chen, O. R. Bilal, K. Shea, C. Daraio, *Proc. Natl. Acad. Sci. USA* **2018**, *115*, 5698.
[22] Y. Chi, Y. Hong, Y. Zhao, Y. Li, J. Yin, *Sci. Adv.* **2022**, *8*, eadd3788.
[23] G. Kang, C. A. H. Allard, W. A. Valencia-Montoya, L. van Giesen, J. J. Kim, P. B. Kilian, X. Bai, N. W. Bellono, R. E. Hibbs, *Nature* **2023**, *616*, 378.
[24] E. Yong, *Nature* **2013**.
[25] J. A. Chamberlain, *Locomotion of Nautilus*, Springer Netherlands, Dordrecht, ISBN 978-90-481-3299-7, **2010**, pp. 489–525.
[26] A. Packard, Q. Bone, M. Hignette, *J. Mar. Biolog. Assoc. U.K.* **1980**, *60*, 313.
[27] R. L. Dupont, Y. Xu, A. Borbora, X. Wang, F. Azadi, K. Havener, B. Lewis, W. Deng, B. W. Tan, S. Li, R. Zhang, Y. Yao, U. Manna, X. Wang, *Adv. Mater.* **2025**, *37*, 9.

[28] X. Lyu, H. Zhang, S. Shen, Y. Gong, P. Zhou, Z. Zou, *Adv. Mater.* **2024**, *36*, 45.
[29] Q. Wang, X. Tian, D. Zhang, Y. Zhou, W. Yan, D. Li, *Nat. Commun.* **2023**, *14*, 3869.
[30] P. Rothemund, N. Kellaris, S. K. Mitchell, E. Acome, C. Keplinger, *Adv. Mater.* **2021**, *33*, 2003375.
[31] D. Wang, F. Zhang, S. Zhang, D. Liu, J. Li, W. Chen, J. Deng, Y. Liu, *Adv. Sci.* **2024**, *11*, 2406956.
[32] Y. Wang, H. Xuan, L. Zhang, H. Huang, R. E. Neisiany, H. Zhang, S. Gu, Q. Guan, Z. You, *Adv. Mater.* **2024**, *36*, 2313761.
[33] J. Zhang, T. Zhang, E. Dong, C. Zhang, Z. Lin, Z. Song, H. Li, N. X. Fang, Y. Zhang, *Cell Rep. Phys. Sci.* **2022**, *3*, 101081.
[34] Y. Wang, P. Zhang, H. Huang, J. Zhu, *Soft Rob.* **2023**, *10*, 590.
[35] V. Maurin, Y. Chang, Q. Ze, S. Leanza, J. Wang, R. R. Zhao, *Adv. Mater.* **2024**, *36*, 2302765.
[36] X. Li, D. Rao, M. Zhang, Y. Xue, X. Cao, S. Yin, J.-W. Wong, F. Zhou, T.-W. Wong, X. Yang, T. Li, *Cell Rep. Phys. Sci.* **2024**, *5*, 101957.
[37] S. Chen, H. Xu, X. Xiong, B. Lu, in *2023 IEEE International Conference on Robotics and Automation (ICRA)*, **2023**, pp. 2613–2619.
[38] F. Gao, Z. Wang, Y. Wang, Y. Wang, J. Li, *J. Bionic Eng.* **2014**, *11*, 412.
[39] Z. Yang, D. Chen, D. J. Levine, C. Sung, *IEEE Rob. Autom. Lett.* **2021**, *6*, 7145.
[40] S. Firouznia, C. Xu, H. Philamore, J. Rossiter, in *2023 IEEE International Conference on Soft Robotics (RoboSoft)*, **2023**, pp. 1–6.
[41] H. Qing, J. Guo, Y. Zhu, Y. Chi, Y. Hong, D. Quinn, H. Dong, J. Yin, *Sci. Adv.* **2024**, *10*, eadq4222.
[42] X. Yang, Y. Chen, T. Chen, J. Li, Y. Wang, *Adv. Mater.* **2024**, *36*, 2404502.
[43] M. A. Fernandes, S. Jadhav, H. Chen, S. Fong, M. T. Tolley, *Front. Rob. AI* **2022**, *9*.
[44] Y. Wei, F. Pan, X. Lin, L. Zhang, J. Xiang, Y. Chen, *Adv. Mater.* **2024**, 2410865.
[45] C. Tang, W. Ma, B. Li, M. Jin, H. Chen, *Adv. Eng. Mater.* **2020**, *22*, 1901130.
[46] Z. Zhang, Z. Xu, L. Emu, P. Wei, S. Chen, Z. Zhai, L. Kong, Y. Wang, H. Jiang, *Nat. Mach. Intell.* **2023**, *5*, 643.
[47] Y. Wang, Q. He, Z. Wang, S. Zhang, C. Li, Z. Wang, Y.-L. Park, S. Cai, *Adv. Mater.* **2023**, *35*, 2211283.
[48] C. Zhang, H. Yang, R. Garziera, Y. Xu, H. Jiang, *Int. J. Mech. Sci.* **2025**, *286*, 109889.
[49] Y. Chi, Y. Li, Y. Zhao, Y. Hong, Y. Tang, J. Yin, *Adv. Mater.* **2022**, *34*, 2110384.
[50] D. Tang, C. Zhang, C. Pan, H. Hu, H. Sun, H. Dai, J. Fu, C. Majidi, P. Zhao, *Sci. Rob.* **2024**, *9*, eadm8484.
[51] G. Li, X. Chen, F. Zhou, Y. Liang, Y. Xiao, X. Cao, Z. Zhang, M. Zhang, B. Wu, S. Yin, Y. Xu, H. Fan, Z. Chen, W. Song, W. Yang, B. Pan, J. Hou, W. Zou, S. He, X. Yang, G. Mao, Z. Jia, H. Zhou, T. Li, W. Yang, *Nature* **2021**, *591*, 66.
[52] G. Li, T.-W. Wong, B. Shih, C. Guo, L. Wang, J. Liu, T. Wang, X. Liu, J. Yan, B. Wu, F. Yu, Y. Chen, Y. Liang, Y. Xue, C. Wang, S. He, L. Wen, M. T. Tolley, A.-M. Zhang, C. Laschi, T. Li, *Nat. Commun.* **2023**, *14*, 7097.
[53] W. Chen, D. Tong, L. Meng, B. Tan, R. Lan, Q. Zhang, H. Yang, C. Wang, K. Liu, *Adv. Mater.* **2024**, *36*, 2400763.
[54] W. Chen, R. Wang, K. Liu, *Mech. Mater.* **2024**, *189*, 104879.
[55] J. Madden, N. Vandesteeg, P. Anquetil, P. Madden, A. Takshi, R. Pytel, S. Lafontaine, P. Wieringa, P. Wieringa, *IEEE J. Ocean. Eng.* **2004**, *29*, 706.
[56] J. E. Hall, *Guyton and Hall Textbook of Medical Physiology*, 13th edn., Guyton and Hall Textbook of Medical Physiology, **2016**.
[57] R. Mittal, H. Dong, M. Bozkurttas, F. Najjar, A. Vargas, A. von Loebbecke, *J. Comput. Phys.* **2008**, *227*, 4825.